ORIGINAL ARTICLE

Interdependent factors influencing the carbon yield, structure, and CO$_2$ adsorption capacity of lignocellulose-derived carbon fibers using multiple linear regression

Isaac Y. Miranda-Valdez[1] · Chamseddine Guizani[1,2] · Nathalie Abbrederis[1] · Mikaela Trogen[1] · Michael Hummel[1]

Abstract

Cellulose has experienced a renaissance as a precursor for carbon fibers (CFs). However, cellulose possesses intrinsic challenges as precursor substrate such as typically low carbon yield. This study examines the interplay of strategies to increase the carbonization yield of (ligno-) cellulosic fibers manufactured via a coagulation process. Using Design of Experiments, this article assesses the individual and combined effects of diammonium hydrogen phosphate (DAP), lignin, and CO$_2$ activation on the carbonization yield and properties of cellulose-based carbon fibers. Synergistic effects are identified using the response surface methodology. This paper evidences that DAP and lignin could affect cellulose pyrolysis positively in terms of carbonization yield. Nevertheless, DAP and lignin do not have an additive effect on increasing the yield. In fact, combined DAP and lignin can affect negatively the carbonization yield within a certain composition range. Further, the thermogravimetric CO$_2$ adsorption of the respective CFs was measured, showing relatively high values (ca. 2 mmol/g) at unsaturated pressure conditions. The CFs were microporous materials with potential applications in gas separation membranes and CO$_2$ storage systems.

Graphical abstract
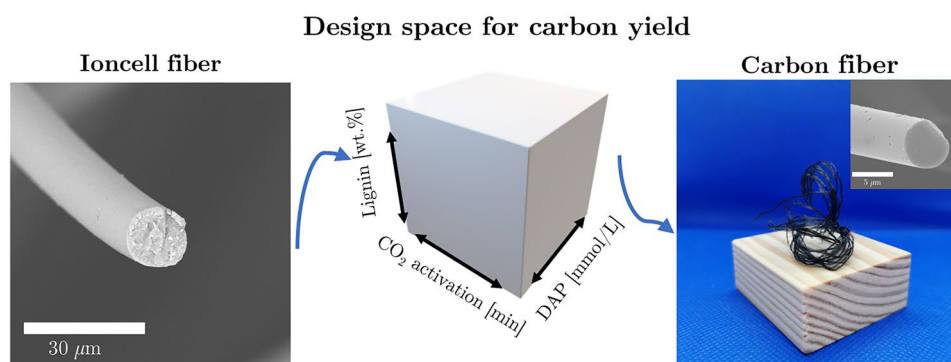
Design space for carbon yield
Ioncell fiber
Carbon fiber

1 Introduction

The ongoing transition toward a widespread bioeconomy in Europe has made cellulose one of the key local raw materials [17, 60, 64]. Demonstrated by the current European single-use plastics directive [18], today cellulose is used for foams [35, 38, 55], textiles [45, 48, 67], packaging [23, 25, 69], and electronics [36, 53, 56]. The wide use of cellulose derives from its local abundance, renewability, and biodegradability. Cellulose has been gaining attention as a potential precursor for carbon material production, especially considering the non-renewable nature of fossil fuels and graphite. Recent research has delved into this topic [14,

Extended author information available on the last page of the article

27, 33]. Significant attention has been devoted to utilizing the thermal decomposition of manufactured cellulose fibers (MCFs), such as viscose and Lyocell fibers, to produce activated carbon fibers (ACFs) for a variety of uses, both structural and non-structural [9, 10]. However, the scalability of cellulose-based carbon fibers (CFs) is hindered by the low carbonization yield of cellulose [70].

The theoretical carbon yield of cellulose accounts for 44.4%, with water being the only gaseous product during cellulose pyrolysis [11, 20]. However, pyrolysis leads to other volatile carbonaceous gases (e.g., CO_2 and CO), which lower the actual carbon yield significantly [30, 66, 76]. For example, typical yields from cellulose pyrolysis are closer to 10% [9, 10, 70]; a yield drastically lower than that derived from polyacrylonitrile (PAN), the most common CF precursor (59%) [50, 77].

In the literature, multiple research papers have addressed the carbonization yield of MCFs [9, 10, 58, 70, 76, 79]. Among the approaches to increase the yield, impregnating fibers with dehydration catalysts, e.g., diammonium hydrogen phosphate (DAP) or diammonium sulfate, before carbonization is a common strategy [9, 32, 76]. Catalysts of this nature promote the dehydration of cellulose and suppress the formation of flammable volatiles such as CO_2, CO, methane, or levoglucosan [58, 76]. Furthermore, at higher temperatures, the heteroatoms present in the catalyst can create covalent bonds and crosslink with the intermediate pyrolysis products, hampering the cleavage of the carbon chains [58, 76]. The carbonization yield of impregnated MCFs has been reported to increase up to 25% compared to the typical 10% yield observed in practice [6, 7, 9, 31, 76].

In a recent study, we increased the carbonization yield of Ioncell MCFs by blending the cellulose substrate with lignin [70]. The effect of lignin on the carbonization yield of CF precursors was first assessed by Oroumei et al. [50]. The authors described having increased the carbonization yield of PAN after blending the polymer with (sulfur-free) organosolv lignin. For the cellulose/lignin blend, we previously reported that respective mixtures showed a carbonization yield of 25% attributed to an additive effect of the carbonization yield of lignin, which is superior to the practical carbonization yield of cellulose [44, 70].

The two aforementioned methods, using either dehydration catalysts or lignin, can compromise the mechanical performance of the resulting CFs. In the first case, DAP promotes micropores in the carbon material [9]. Lignin reduces the long-range crystallinity of cellulose, increasing the disorder in the precursor fiber [33]. A typical procedure to improve the carbonization yield and structural defects of the CFs entails activating the carbon material. Through the development of microporosity and functional sites, ACFs have shown interesting properties in energy storage systems (ESS) and the adsorption of toxic substances [8, 9, 14]. For

instance, Breitenbach et al. [9] made an ACF electrode from carbonizing impregnated viscose fibers.

This work assessed the influence of lignin, DAP, and physical activation on the carbonization yield and CF properties. Following the individual effects of dehydration catalysts and lignin on the carbonization yield of cellulose, we address investigating whether these two substances have a cooperative effect when combined. Additionally, we measured the performance of the manufactured CFs and ACFs regarding CO_2 adsorption to elucidate a potential non-structural application for these fibers and other potential applications typical of carbon materials [71, 74, 75].

2 Materials and methods

Ioncell precursor fibers with and without lignin were prepared as described earlier [70]. In short, Enocell dissolving-grade pulp (cellulose content: 91.7%, hemicellulose: 7.7%) was used as cellulose source and blended with organosolv beech lignin (BL). Three types of fibers were produced: (a) E100, (b) E70, and (c) E50 with the number referring to the weight content of cellulose. For example, E70 is a fiber made up of 70 wt.% cellulose, where the remaining 30 wt.% correspond to the lignin content. Filaments were spun at a draw ratio of 6, resulting in fibers of ca. 15 μm diameter. The fibers were cut into 9 cm long pieces. For a detailed description of the Ioncell spinning process, the reader is directed to articles published by Ma et al. [39], Sixta et al. [62], Asaadi et al. [3]. The coagulated cellulose in the Ioncell fibers showed a weight average molecular weight (Mw) of 130 kDa and a polydispersity index of 2.7. Protocol and equipment to determine the molar mass distribution of the carbohydrate fraction followed Pitkänen and Sixta [52], who reported using 9.0% LiCl in DMAc rather than 0.9%. DAP (reagent grade $\geq$ 98%) was obtained from Sigma-Aldrich (India). The solubilized catalyst was prepared using deionized water.

2.1 Experimental design

The CF yield ($\hat{y}$) was modeled as a function of three independent factors (k): the molar concentration of DAP in the impregnation solution (x_1), CO_2 activation time (x_2), and lignin content in the Ioncell fiber (x_3). Therefore, the experimental design was limited to the space limitations of a tridimensional FCCD, calculating the number of sampling points (N) according to Eq. 1. The FCCD provided a framework for analyzing the inter-dependency between the factors and their effects on $\hat{y}$ at low, medium, and high levels. In addition, a triplicate was chosen at the center point (n) to assess the statistical dispersion of the results. Creating and analyzing the FCCD was assisted by using the Design of Experiments app integrated into OriginPro® 2021b. Table 1 shows the

Table 1 Sampling points of the Face-centered Central Composite Design

Sample	DAP (mmol/L)	CO$_2$ activation (min)	Lignin (wt.%)
N1	0	0	0
N2	40	0	0
N3	0	40	0
N4	40	40	0
N5	0	0	50
N6	40	0	50
N7	0	40	50
N8	40	40	50
N9	0	20	30
N10	40	20	30
N11	20	0	30
N12	20	40	30
N13	20	20	0
N14	20	20	50
N15	20	20	30
N16	20	20	30
N17	20	20	30

For the design matrix, the minimum and maximum levels for each factor were manually inputted, as well as the medium level for the lignin content. The factorial points in the design matrix are experiments N1 to N8, while N9 to N14 represent star points. The last three experiments are replicates located at the center point

sampling points of the design matrix. The minimum and maximum of the DAP concentration were fixed based on the concentration ranges suggested in the literature to improve the carbonization yield [8]. CO$_2$ activation times were chosen based on thermogravimetric analyses on the fibers, see Figure S4. After 40 min, the carbon yield of some fibers was too low for characterization. Finally, the limits for the lignin concentrations were selected based on the results reported by Trogen et al. [70]. In other words, 30 and 50 wt.% lignin show a noticeable effect on increasing the carbon yield of the fibers.

$$N = 2^k + 2k + n \qquad N = 17 \tag{1}$$

Equation 1 yields 17 experiments. In other words, eight factorial points, six star points, and three center points. Equation S1 describes the model used to analyze $\hat{y}$.

2.2 Preparation of the activated carbon fibers

The impregnation protocol followed procedures described in the literature [7, 9, 24, 76, 78]. First, all the precursor fibers were immersed in aqueous solutions containing the respective molar concentrations of the catalyst (Table 1). To be more precise, the process of impregnation involved the

dissolution of DAP in water for 10 min while being stirred magnetically at room temperature. Following this step, 1.2 g of fibers were immersed for 2 h in the freshly prepared solutions (1:200 weight ratio). Then, the soaked fibers were dried overnight at 105 °C in a convection oven, VENTI-Line® (VWR, Germany), to remove the excess liquid.

Once dried, carbonization and CO$_2$ activation of the fibers took place in a tube furnace Nabertherm RHTH 80-300/16 (Germany). Two samples were heated simultaneously to 800 °C (5 °C/min) in an N$_2$ gas (flow rate: 120 L/h) atmosphere. Before heating, N$_2$ gas was purged through the furnace for 15 min. After having reached 800 °C, the temperature was kept for half an hour, and then CO$_2$ gas (flow rate: 120 L/h) was added to reach the same N$_2$ gas flow rate. CO$_2$ gas flowed for the respective activation time of each sample and was then reduced to zero. Then, the fibers were held in the furnace until they reached 100 °C (under N$_2$ gas atmosphere). The flowchart in Fig. S1 illustrates the sequence to prepare the activated carbon fibers. Lastly, the CF yield was measured after having considered the initial fiber mass put in the furnace and the mass after heat treating them.

2.3 Thermogravimetry

The thermal decomposition of Ioncell fibers with DAP and lignin was studied using a thermogravimetric analyzer from Netzsch STA 449 F3 Jupiter in Germany. The purpose was to evaluate the impact of temperature and CO$_2$ activation on CF yield under carbonization conditions in a tube furnace. The experiment involved heating the samples from 40 to 800 °C (5 °C/min) with a constant flow of N$_2$ gas (60 ml/min). Then, at 800 °C, the samples were held at that temperature for 30 min; then, CO$_2$ gas flow (60 ml/min) was injected to match the conditions of the protective atmosphere. The oxidizing atmosphere was maintained for two hours, and the mass loss was recorded throughout the entire procedure.

2.4 Textural characterization

At a temperature of −196 °C, the N$_2$ physisorption capacity was measured. The CF samples were cut into short threads that were less than 5 mm in length for analysis. To degas the samples, N$_2$ gas was used at a temperature of 150 °C for a period of 12 h. An analyzer called the Micromeritics TriStar II 3020 (United States) was then employed to gradually increase the relative pressure (p/p_0) and register the loaded adsorbate, thereby creating the adsorption isotherms. Using a Python^{TM}-based framework named "pyGAPS" [26], the BET surface area (a_s) and microporosity volume of each sample were estimated. It is worth noting that Osterrieth et al. [51] recently highlighted the wide statistical dispersion associated with treating N$_2$ adsorption data. This dispersion arises due to different procedures used to calculate textural properties like the

BET surface area a_s. To standardize the procedure for calculating a_s and microporosity volume (V_μ), the Rouquerol [57] and t-plot (non-porous carbon as reference) methods were used, respectively, by pyGAPS for this study.

2.5 Raman spectroscopy

The CF samples were analyzed using an inVia^{TM} Raman microscope Renishaw® Qontor (United Kingdom) using a green laser ($\lambda = 532$ nm and 10% intensity) and a 20× objective within a Raman shift wavenumber (ω) range from 850 to 1930 cm^{-1}. The interval was scanned 30 times. Each spectrum was the average of three measurements at different spots. The background was subtracted from all the spectra using the intelligent baseline subtraction tool of WiRE^{TM} 5.1 (first-degree function as baseline).

As proposed in the literature [40, 41, 46], we analyzed the CF spectra by applying a three-peak decomposition of the D and G bands. The D band was fitted with two Gaussian functions centered at the same spectral position, and a Breit-Wigner-Fano (BWF) was used to fit the G band. One of the most widely accepted approaches for fitting the Raman spectra of disordered carbons involves the use of three peaks [40, 41, 46]. The former stems from the meaningful parameters, which compose the cumulative fitting function presented in Eq. 2 [40, 41, 46]. In Eq. 2, I is the intensity as a function of ω. There, ω_D and ω_G represent the D and G band phonons. Γ_{D_1} and Γ_{D_2} are the bandwidths of the two D sub-bands, while Γ_G represents the width of the G band. q represents a coupling factor of the BWF function. To determine the average crystallite diameter in the basal plane (L_a) using the I_D/I_G ratios, we employed Ferrari's and Robertson's law (Eq. 3) [19]. Being the D band decomposed into two sub-bands with the same phonon, the sum $I_{D_1} + I_{D_2}$ yields the parameter I_D. In Eq. 3, E_L is the laser energy in eV (2.33 eV), and α is the exponent to be calculated. For graphene, α is 4 [12].

$$I(\omega) = I_{D_1} e^{\frac{(\omega-\omega_D)^2}{2\Gamma_{D_1}^2}} + I_{D_2} e^{\frac{(\omega-\omega_D)^2}{2\Gamma_{D_2}^2}} + I_G \frac{\left(1 + \frac{\omega-\omega_G}{q\Gamma_G}\right)^2}{1 + \left(\frac{\omega-\omega_G}{\Gamma_G}\right)^2} \quad (2)$$

$$L_a = \sqrt{\frac{\frac{I_D}{I_G}}{0.55 \times \left(\frac{2.41}{E_L}\right)^\alpha}} \quad (3)$$

2.6 Scanning electron microscopy

A Field Emission Scanning Electron Microscope (FE-SEM) Zeiss Sigma VP from Germany was used for inspecting the CF surface. The samples were cut into small segments and coated with a gold-palladium 80/20 alloy before imaging the CF. The coated CF was mounted on carbon adhesive tape and placed under high vacuum. To observe their longitudinal sections, the fibers were laid horizontally on the sample holder. An electric potential ranging from 5 to 9 keV was required for imaging the CFs. In some selected cases, the analyses were accompanied by Energy-Dispersive Spectroscopy (EDS) using Ultim Max from Oxford Instruments.

2.7 Carbon fibers performance in CO_2 adsorption

This paper evaluated the ability of CF to adsorb CO_2 without affecting the structure. The experiments were conducted using the methodology described by Ojwang et al. [49]. Thermogravimetric CO_2 gas adsorption tests were selected, and 13–15 mg of CF was mounted in a thermogravimetric analyzer STA 449 F3 Jupiter, Netzsch (Germany). The experimental procedure involved degassing the CF at 150 °C for an hour under He gas flow (200 ml/min). Then, the temperature was reduced to 40 °C, and the samples remained under the same gas flow for two hours to stabilize the temperature. The adsorption and desorption process was carried out gradually and step-wise by replacing the atmosphere from He to CO_2. Figure S2 shows the gas exchanging process and CO_2 loading recorded during the experiment. Finally, CO_2 adsorption and desorption isotherms were plotted from the experimental data after weight-averaging the loaded adsorbate at each step indicated in Fig. S2.

2.8 X-ray photoelectron spectroscopy

To analyze the effect of oxygen-containing functional groups on CO_2 adsorption, five CF samples were chosen for examination. These samples, named N4, N7, N8, N11, and N16, underwent X-ray photoelectron spectroscopy (XPS). The XPS analysis was performed with a Kratos AXIS Ultra DLD X-ray photoelectron spectrometer utilizing a monochromated Al$_{k\alpha}$ X-ray source (1486.7 eV) at 100 W. The XPS spectra were obtained with a pass energy of 80 eV and a step size of 1.0 eV. In contrast, collecting high-resolution spectra necessitated a pass energy of 20 eV and a step size of 0.1 eV. High vacuum conditions were used to acquire photoelectron signals at a take-off angle of 90 °C. The X-ray beam had a diameter of 1 mm, and the analysis area was 300×700 µm. The XPS spectra were collected at three different spots in the samples, and all of them were charge-corrected based on the position of the graphitic bonding of carbon at 284.2 eV.

3 Results and discussion

Carbon fibers were produced from Ioncell cellulose fibers and the experimentally observed CF yields ($\hat{y}$) were fitted to the model described by Eq. S1 using multiple linear regression (MLR) in OriginPro 2021b. In the first trial, the factor CO_2 activation time showed a negligible effect on $\hat{y}$. However, knowing that the activation process should contribute to the increase in sample burn-off [5], we reviewed the effect of the oxidizing atmosphere on $\hat{y}$ before continuing with further experimentation. Therefore, it was found that during CO_2 activation, the initial Ioncell fibers shape (ca. 9 cm long fiber bundles) hindered CO_2 diffusion from the gas atmosphere into the bulk matrix. The described phenomenon led to an ineffective activation via the Boudouard reaction [65]. To circumvent this experimental impediment, the CFs were cut into fragments smaller than 5 mm, and samples with activation times were reactivated by following the procedure in Fig. S1.

After reactivating the fibers, Eq. S1 successfully fitted the experimental $\hat{y}$ and gave the coefficients in Table 2. In addition, Fig. S3 compares the observed and predicted $\hat{y}$; the regression model that fitted the experimental results led to a coefficient of determination (R^2) of ~0.993. From the model, the quadratic term (b_{22}) for the CO_2 activation time was removed due to it was indistinguishable from noise. Analyzing the effects of each factor on $\hat{y}$ revealed a positive

Table 2 Carbonization yields and properties of the CF samples composing the Face-centered Central Composite Design

Sample	$\hat{y}$ (%)	a_s (m²/g)	V_μ (cm³/g)	L_a (nm)	CO_2 load [a] (mmol/g)
N1	13.51	–	–	1.20	1.65
N2	24.73	–	–	1.19	1.67
N3	10.91	671	0.258	1.25	1.83
N4	22.56	576	0.219	1.29	1.80
N5	25.71	–	–	1.20	1.53
N6	27.30	–	–	1.19	1.63
N7	21.83	613	0.230	1.26	1.90
N8	24.84	524	0.199	1.26	1.72
N9	17.73	515	0.195	1.25	1.59
N10	22.72	434	0.164	1.22	1.68
N11	20.80	–	–	1.08	1.45
N12	18.86	526	0.199	1.24	1.75
N13	17.33	472	0.178	1.22	1.70
N14	23.91	484	0.184	1.24	1.66
N15	18.90	503	0.190	1.22	1.69
N16	18.54	483	0.184	1.25	1.79
N17	19.12	474	0.181	1.27	1.69

[a]Adsorption at $p/p_{atm} = 0.75$

influence of both DAP and lignin on the average yield $\hat{y}$. However, this increase was more noticeable when the precursor fibers contained only one of them. The negative coefficient b_{13} implies that the combination of DAP and lignin had a minor synergistic effect on increasing $\hat{y}$. The independent effects of DAP and lignin, respectively, were anticipated. Breitenbach et al. [9] have recently reported a yield of 34.6% by impregnating viscose fibers with a solution of 56 mmol/L DAP. Similarly, Bai et al. [6] reported that the carbonization yield of DAP-impregnated Lyocell fibers increased from 19 to 23%. The effect of lignin on $\hat{y}$ was already addressed earlier in this discussion [70].

The enhanced yield promoted by adding DAP to Ioncell fibers was to be expected. DAP is known to promote the dehydration of cellulose, reducing the amount of volatile and flammable carbonaceous compounds [76]. Zeng and Pan [76] pointed out that remaining traces of DAP or condensation products thereof with cellulose can lead to an apparent increase in the CF yield. To assess this effect, we performed an EDS analysis on sample N10. The EDS results in Fig. 1 showed a residual DAP content in a few CF segments. Therefore, the remaining products of DAP should be considered when using DAP as a carbonization catalyst. Concerning the effect of lignin on $\hat{y}$, Ioncell fiber blends (E70 and E50) decomposed slowly over a broad temperature range [70]. Above 200 °C, lignin pyrolysis promotes a melt phase radical process, consisting of initiation, propagation, and termination reactions [70]. These reactions have a similar effect as observed for DAP; lignin and DAP can have an oxidative effect on the precursor fiber [70, 76]. Oxidation of the precursor fibers at low temperature (not to be confused with activation) creates cross-links and olefinic moieties, reducing the probability of forming volatile compounds during the heat treatment [42].

In contrast, CO_2 activation time impacted negatively on $\hat{y}$. The negative sign of b_2 is in agreement with the literature; the sample burn-off (gasified carbon) increases by increasing the CO_2 activation time [5, 9]. Nonetheless, the interactions between CO_2 gas, DAP, and lignin had mixed effects on $\hat{y}$. First, when the precursor fibers contain DAP, a positive coefficient b_{12} denotes a low reactivity between CF and CO_2. Similar trends were observed by Breitenbach et al. [9] and Zeng and Pan [76]. For example, a concentration interval in which DAP and CO_2 activation increase carbonization yield was reported. Another aspect to consider is the presence of inorganic elements, such as phosphorous, which may have hindered the gasification kinetics [16]. The former statements may also explain the extended area in the contour plot in Fig. 2, where the CO_2 activation does not drop the yield below 22% when increasing the activation time and fixing the DAP concentration to 40 mmol/L.

The interaction between lignin and CO_2 activation time, represented by b_{23}, shows that CO_2 gas tends to react with

Fig. 1 Energy-Dispersive Spectroscopy mapping of **a** carbon, **b** oxygen, and **c** phosphorus in sample N10 (30% lignin, 40 mmol/L DAP, 20 min CO_2 activation). The average composition of the **d** scanned zone accounted for 89.7% C, 7.6% O_2, and 2.7% P
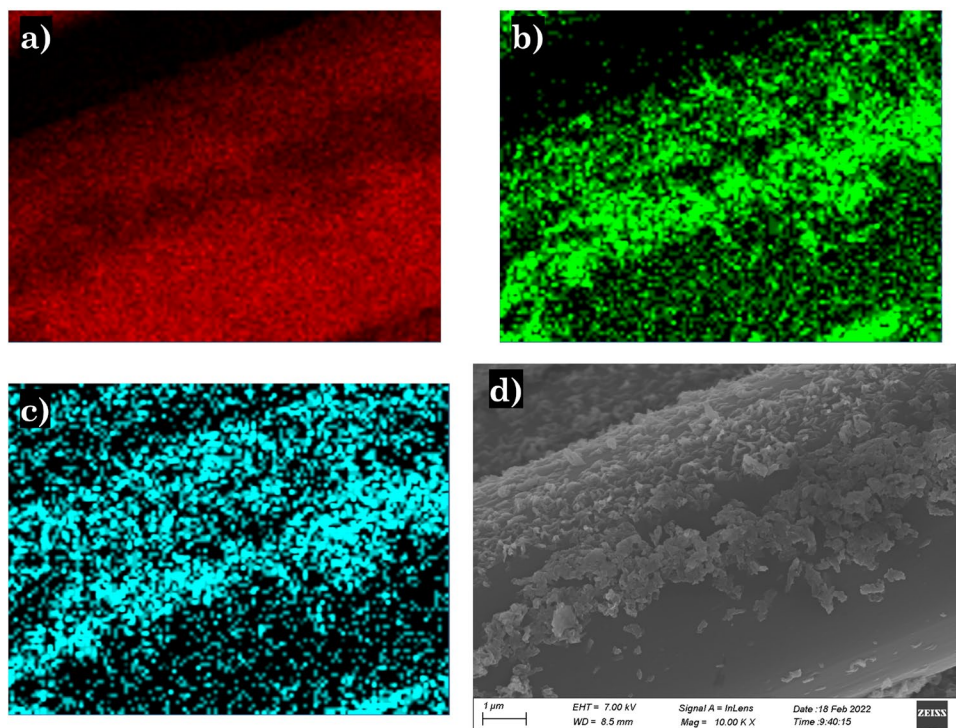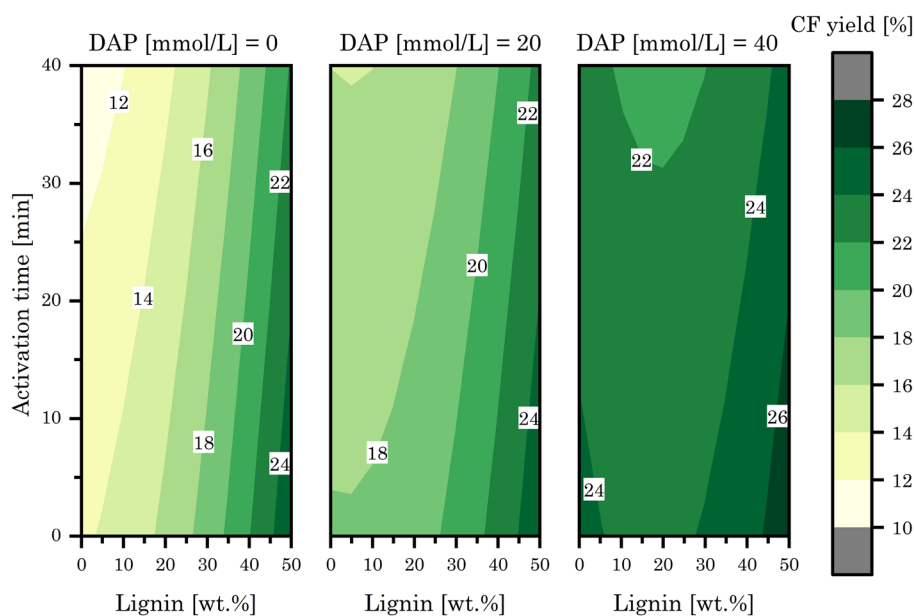

Fig. 2 4-D contour plot of the predicted response surface interactions and cumulative effects of diammonium hydrogen phosphate, lignin, and CO_2 activation time on the carbonization yield. The plot results from a Multiple Linear Regression applied to the observed carbonization yields, $R^2 = 0.993$

the carbon produced after lignin pyrolysis. However, b_{23} should not be overinterpreted as its standard error is high. After evaluating the physical meaning of the model, we made the contour plot in Fig. 2. In Fig. 2, the highest $\hat{y}$ stems from mixing DAP and lignin in their maxima. Nonetheless, this yield is 2% higher than predicted and observed from the individual effects of adding DAP or lignin at their highest levels. As mentioned before, the negative coefficient b_{13} means that the combination of DAP and lignin does not

grant an increase of $\hat{y}$. The pyrolysis of lignin and DAP are melt-phase processes [70]. Thus, the interactions of DAP and lignin in the liquid transition state may affect the interaction between DAP and cellulose.

In order to gain a better understanding of the mass loss that occurs during carbonization, we analyzed selected thermogravimetric results as shown in Fig. S4. Our observations for samples E100, E70, and E50 were similar to those reported by Trogen et al. [70]. When cellulose is combined

with lignin, the yield of Ioncell fibers during carbonization is increased. Similarly, the inclusion of a dehydration catalyst in the precursor fibers has a comparable effect to tube furnace carbonizations. A lower carbonization yield was discovered in sample E70/DAP in comparison to samples E100/DAP, indicating that the combination of lignin and DAP does not enhance carbonization yield. However, the addition of lignin and DAP in higher concentrations (E50/DAP) resulted in an increased yield, which was also observed during tube furnace carbonizations. Finally, Fig. S4 illustrates the mass loss behavior during CO_2 activation. The CO_2 activation segment for all samples containing DAP exhibited a slight mass loss of approximately 1.5%, consistent with our earlier interpretation that residual catalyst on the CF surface may hinder solid carbon gasification due to lower reactivity when precursor fibers contain DAP.

3.1 Textural characterization

The assessment of activated carbon texture using the BET specific surface area (a_s) parameter has been a topic of debate in previous years, according to sources such as Shi [61], Marsh and Rodríguez-Reinoso [42]. However, the focus of this research is on the unclear approach to calculating a_s, as highlighted by Osterrieth et al. [51]. To address this problem, the N_2 adsorption isotherms in this study were analyzed using "pyGAPS", a framework based on Python which processes adsorption isotherms, as developed by Iacomi and Llewellyn [26]. The goal of pyGAPS is to standardize the mathematical processes involved in analyzing adsorption isotherms. To compare the results of pyGAPS with another Python-based framework, "betsi-gui," which uses the Rouquerol criteria to calculate BET surface areas, this research processed adsorption isotherms with both tools [54]. The conclusion of this study was that pyGAPS and betsi-gui produced the same results, demonstrating the usefulness of both tools in standardizing the process.

For our analyses, we opted to use pyGAPS since it offers a variety of algorithms that can calculate different textural properties, such as V_μ. The outcomes of our isotherm processing are outlined in Table 2. Any CF samples lacking an activation protocol, as depicted in Fig. 3, did not show any detectable N_2 physisorption. This resulted in some missing data for a_s and V_μ in Table 2. The isotherms (Fig. 3) showed substantial gas adsorption at low relative pressures ($p/p_0 < 0.1$), followed by a sharp knee, ultimately leading to asymptotic gas adsorption at its highest point. This type of adsorption behavior corresponds to the IUPAC classification type I(a), which is generally found in microporous materials [68]. The lack of adsorption data observed in the unactivated samples can be explained by the microporous nature of the CF studied. The diffusion kinetics of N_2 molecules into the solid carbon faces limitations due to the narrow pore size
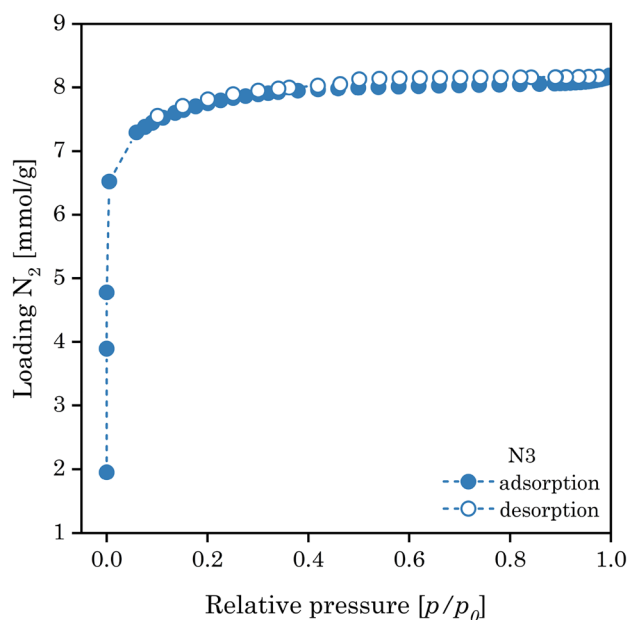

Fig. 3 Nitrogen adsorption and desorption isotherms measured for the samples in the Face-centered Central Composite Design. The x-axis on each plot shows the relative pressure (p/p_0) and the y-axis indicates the N_2 load in mmol/g

(< 2 nm) at the experimental temperature (− 196 °C) [22]. To overcome this diffusion constraint, a few authors have proposed supplementing N_2 adsorption with CO_2 adsorption isotherms at room temperature [1, 2, 22].

To evaluate the relation between a_s and V_μ, Fig. S6 illustrates a comparison between these textural properties. We observed in the literature that the criticism toward a_s comes from its deficiency to include the effect of microporosity on the surface area of activated carbons [42, 61]. Particularly, this controversy considers that micropores and mesopores have different adsorption capacities [61]. Nevertheless, for the studied CF, Fig. S6 demonstrates that a_s comes mainly from the formation of microporosity since the scatter points align linearly. Therefore, a_s is a sensible property for the studied microporous CF to characterize the material texture.

3.2 Raman spectroscopy

When non-graphitizable precursors like cellulose and lignin are carbonized, they result in disordered carbon structures that are made up of graphene layers. These structures lack higher-order orientation [46, 47]. According to Oberlin [47], at low pyrolysis temperatures (< 600 °C), cross-linking reactions take place in cellulose and lignin, which can impede the formation of graphene stacks. This can result in a relatively small average crystal size L_a [46]. The Ioncell CF under study is expected to have turbostratic structures due to its non-graphitizable nature and the inclusion of DAP in

the precursor fibers. DAP is known to introduce cross-linked functionalities that prevent the release of small volatile carbon compounds [76]. Figure 4 illustrates the experimental and fitted Raman spectra of all the studied CF specimens. The maxima of the sp2 C bonding excitation known as G band were at $\omega \approx 1590–1594$ cm^{-1}. Alternatively, the D band (formation of six-fold aromatic rings and point defects) had their maxima at $\omega \approx 1337–1346$ cm^{-1} [19, 46]. According to Ferrari and Robertson [19], the D band intensity (I_D) could be directly proportional to the probability of finding long-range polyaromatic structures in the CF. Therefore I_D/I_G ratio is one procedure which estimates the crystallite size L_a [19, 40, 41, 46].

We utilized the methodology proposed by various researchers, including Mallet-Ladeira et al. [40, 41] and Mubari et al. [46], to calculate the parameter L_a for each CF sample. This approach involves deriving the I_D/I_G ratio from a three-peak decomposition of the Raman spectra. To accomplish this, we fit the D band using two Gaussian functions with the peak maximum at the same wave number, while the G band was fitted using a BWF function. While Mallet-Ladeira et al. [40, 41] initially proposed using two Lorentzian functions to deconvolve the D band, we found that in biobased carbons, the presence of a shoulder at 1100–1200 cm^{-1} alters the shape of the D band and
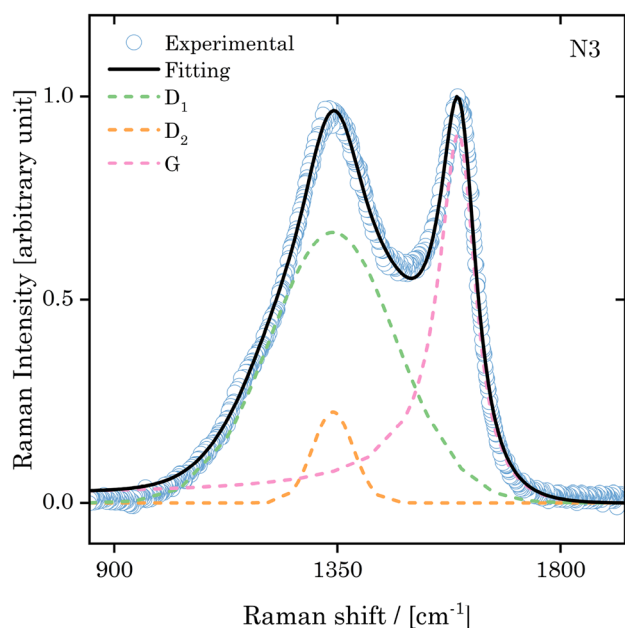

Fig. 4 Raman spectrum of samples N3 (0 mmol/L DAP, 40 min CO_2 activation, and 0 wt.% lignin) and its decomposition using the three bands method. The x-axis in each plot represents the Raman shift wavenumber in cm^{-1}, and the y-axis is the G band normalized Raman intensity in arbitrary units. The solid line depicts the cumulative fit in each spectrum after decomposing the experimental spectrum in three bands: two Gaussian functions at the same wavenumber for the D band and one Breit-Wigner-Fano function for the G band

makes it more Gaussian-like [63]. Additionally, the low carbonization temperature of 800 °C contributes to observing broad D and G bands, which is attributed to a confinement effect in nanomaterials [73]. The BWF function was used to fit the asymmetric G band typical of disordered carbons, which deviates from a perfect Lorentzian as a result of the density of vibrational states [19, 40, 43]. The results of the decomposition process are shown in Fig. 4 and Fig. S7, demonstrating an excellent fit to the experimental data for all spectra with R^2 values ranging between 0.996–0.997.

The crystallite sizes L_a and characteristics of the fitted bands are summarized in Table 2 and Table S2, respectively. Ferrari's and Robertson's law (Eq. 3) was adequate for calculating L_a since the crystal parameter was smaller than 2 nm in all the cases [19]. However, as observed in Table 2, the samples displayed similar L_a values (ca. 1.2 nm) despite their initial compositions. To illustrate these similarities, L_a is plotted against the intensity ratios of the D and G bands in Fig. S8. A reason for the similar L_a sizes could be the maximum carbonization temperature and heating rate effects, which remained the same (800 °C and 5 °C/min) for all sample carbonization (Fig. S1). Modifying the thermal parameters significantly affects the crystal size as the Gibbs free energy and pyrolysis kinetics change. For example, Mubari et al. [46] and Breitenbach et al. [10] reported the effect of the carbonization temperature and heating rate on the crystal size of biobased carbons, respectively. At a higher carbonization temperature and a slower heating rate could increase L_a. The former would explain why the response surface analysis designed herein to analyze would not be suitable for studying L_a. Furthermore, the replicates (N15-N17) showed a significant scatter of the L_a values (Fig. S8).

3.3 Carbon fibers performance in CO₂ adsorption

The CO_2 adsorption and desorption capacity of the CF was estimated via thermogravimetry. Figure 5a depicts the adsorption and desorption isotherms of all the CF samples, and Table 2 the CO_2 adsorption capacities at $p/p_{atm} = 0.75$, respectively. Overall, the isotherms depict almost negligible hysteresis, a characteristic typically observed in ultramicroporous materials [15, 59, 72]. At the experiment temperature (40 °C), hysteresis lacks since there are no kinetic restrictions for CO_2 molecules to move through the narrow micropores [72]. This feature may also indicate that the studied CF physically adsorb CO_2 molecules (physisorption). To assess the physisorption mechanism, we attempted to correlate the CF textural properties with their CO_2 adsorption capacity. Thus, the adsorption isotherms were fitted using Freundlich's equation (Eq. 4), which represents a basic adsorption model [21]. Freundlich's empirical equation describes adsorption as a phenomenon

Fig. 5 a Thermogravimetric CO_2 isotherms (40 °C) of the samples in the Face-centered Central Composite Design. The x-axis in each plot represents the relative pressure p/p_{atm} and the y-axis the CO_2 load in mmol/g. The dotted line represents Freundlich's empirical equation for gas adsorption. **b** Freundlich's empirical parameter C as a function of the BET surface areas a_s of the samples composing the Face-centered Central Composite Design
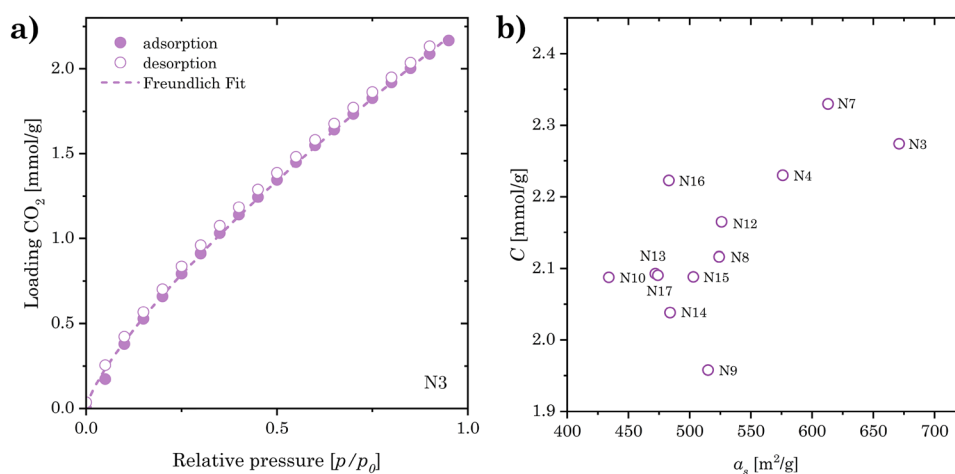
following a power law-like behavior. In Eq. 4, χ is the adsorbate mass divided by the adsorbent mass while C and r are adsorption constants for the pair adsorbate-adsorbent at the experimental temperature.

$$\chi = C\left(\frac{p}{p_{atm}}\right)^{1/r} \tag{4}$$

Jaroniec [28] demonstrated that C could be related to heterogeneities present in the adsorbent, which, in this case, could translate to the CF textural properties. Canevesi et al. [13] have used a modified version of Eq. 4 to assess the effect of texture and surface chemistry of activated carbons on their CO_2 uptake. Hence, Fig. 5b plots the calculated C values as a function of the BET surface areas. Although Fig. 5b shows that the parameter C tends to increase as a function a_s, there is no relationship visible between the empirical parameter C and a_s. Therefore, we conclude that the observed CO_2 adsorption capacity does not depend exclusively on the CF surface area but can also be connected to other factors, as Canevesi et al. [13] have reported. Especially in biobased activated carbons, Ashourirad et al.[4] underlined that CO_2 adsorption capacity depends on both the surface area and oxygen-containing functionalities.

To investigate the potential impact of oxygen content on CO_2 adsorption performance, five samples (N4, N7, N8, N11, and N16) of CF were analyzed using XPS. Table 3 displays the relative concentrations of elements in the samples. All samples exhibited signals for C, N, O, and P, as well as traces of Ca, which is characteristic of biomass products. Based on the results presented in Table 3, it can be concluded that the CO_2 adsorption performance is influenced by the oxygen-containing functionalities present. Specifically, the samples with higher oxygen concentrations exhibited greater CO_2 adsorption. Although the relationship between oxygen functionalities and CO_2 adsorption is commonly overlooked, it is possible that oxygen sites in the CF may increase CO_2 uptake by polarizing and trapping CO_2 adsorbate molecules in the micropores through dipole-dipole and quadrupole van der Waals interactions [4, 29, 34, 37]. Consequently, the observed differences in CF chemistry may explain why CF with a larger surface area did not always exhibit higher CO_2 uptake in some instances. For example, sample N4 had the largest surface area but adsorbed less CO_2 than N7. By examining the precursor chemistry of N7 (Table 2), it is evident that N7 contained lignin, which may have generated more oxygen functionalities in the final CF. Therefore, N7 had a higher CO_2 adsorption capacity than N4. However, this is not a definitive conclusion since

Table 3 Quantitative relative surface chemistry in wt.% estimated from X-ray photoelectron spectroscopy. The BET surface area (a_s) in m^2/g and CO_2 uptake (χ) in mmol/g are presented to remark both texture and surface chemistry effects on the CO_2 adsorption performance

Sample	C 1 s	Ca 2p	N 1 s	O 1 s	P 2p	a_s	χ^a
N4	94.44	0.42	0.11	4.48	0.56	576	1.80
N7	92.48	0.57	0.65	6.30	0.00	613	1.90
N8	93.10	0.64	0.55	4.97	0.74	524	1.72
N11	89.57	1.16	0.44	7.55	1.29	–	1.45
N16	89.11	0.84	0.56	8.55	0.94	483	1.79

[a]Adsorption at $p/p_{atm} = 0.75$

other samples containing lignin (e.g., N8 and N9) showed lower CO_2 adsorption than N4. In summary, all the samples exhibited high CO_2 adsorption at unsaturated conditions (~ 2 mmol/g) that could be utilized in the future to create gas separation membranes and CO_2 storage systems. Additionally, it is important to consider both textural and chemical heterogeneities in the CF when modeling CO_2 uptake.

4 Conclusion

The model successfully assessed the impact of DAP impregnation, CO_2 activation time, and lignin content on the carbonization yield of Ioncell fibers. DAP and lignin could affect cellulose pyrolysis positively in terms of carbonization yield. DAP increased the carbonization yield of the fibers as it is known to promote the dehydration temperature of cellulose and thereby induce cross-links in the emerging carbon structure, reducing the formation of volatile carbonaceous products. Similarly, lignin can alter cellulose pyrolysis when in intimate contact with the fiber matrix and shifts the onset of degradation to higher temperatures. Interpreting the regression coefficients of the carbonization yield model showed that combining DAP and lignin does not have an additive effect on increasing the yield. DAP and lignin can even affect the carbonization yield negatively within a certain composition range, while the CO_2 activation time showed a reduced effect on the carbonization yield. The low reactivity was attributed to mass diffusion constraints at the carbonization conditions and to the presence of cross-linked carbon atoms, which may arise in the CFs upon adding DAP to the precursor fibers. However, a more detailed study of the pyrolysis phases would be necessary to confirm the phenomena. This study also provided answers to existing controversies in the literature. For example, the results showed that, especially in biochars, the precursor chemistry generates oxygen-containing functionalities, which may significantly contribute to the CO_2 uptake capacity of CF. Based on all our findings, we foresee gas separation membranes and CO_2 capture systems as future applications for the studied CF.

Author contributions IYM-V Conceptualization, Methodology, Software, Formal analysis, Investigation, Visualization, Writing—Original draft, Writing—Review and Editing. CG: Conceptualization, Validation, Funding acquisition, Methodology, Formal analysis, Writing—Review and Editing. NA: Investigation. MT: Resources. MH: Conceptualization, Validation, Formal analysis, Writing—Review and Editing, Funding acquisition, Project administration.

Availability of data and materials Data is available upon reasonable request.

Declarations

Conflict of interest On behalf of all authors, the corresponding author states that there is no conflict of interest.

Ethics approval and consent to participate Not applicable.

Consent for publication The authors gave their consent for publication.

References

1. Aleghafouri A, Mohsen-Nia M, Mohajeri A, Mahdyarfar M, Asghari M (2012) Micropore size analysis of activated carbons using nitrogen, carbon dioxide and methane adsorption isotherms: experimental and theoretical studies. Adsorpti Sci Technol 30(4):307–316. https://doi.org/10.1260/0263-6174.30.4.307

2. Almoneef MM, Jedli H, Mbarek M (2021) Experimental study of CO_2 adsorption using activated carbon. Mater Res Express. https://doi.org/10.1088/2053-1591/ac05fe

3. Asaadi S, Hummel M, Ahvenainen P, Gubitosi M, Olsson U, Sixta H (2018) Structural analysis of Ioncell-F fibres from birch wood. Carbohyd Polym 181:893–901. https://doi.org/10.1016/j.carbpol.2017.11.062

4. Ashourirad B, Arab P, Islamoglu T, Cychosz KA, Thommes M, El-Kaderi HM (2016) A cost-effective synthesis of heteroatomdoped porous carbons as efficient CO_2 sorbents. J Mater Chem A 4(38):14693–14702. https://doi.org/10.1039/c6ta06251b

5. Babel K (2003) Porous structure evolution of cellulose carbon fibres during oxidation in carbon dioxide. Adsorpt Sci Technol 21(4):363–371. https://doi.org/10.1260/026361703322405079

6. Bai BC, Kim EA, Jeon YP, Lee CW, In SJ, Lee YS, Im JS (2014) Improved flame-retardant properties of lyocell fiber achieved by phosphorus compound. Mater Lett 135:226–228. https://doi.org/10.1016/j.matlet.2014.07.131

7. Bai BC, Im JS, Lee YS (2017) Lyocell-based activated carbon fibers improved the adsorption of harmful gas properties

when produced via dual-simultaneous treatments. Carbon Lett 23(3):69–73. https://doi.org/10.5714/CL.2017.23.069

8. Bai BC, Lee YS, Im JS (2019) Activated carbon fibers for toxic gas removal based on electrical investigation: mechanistic study of p-type/n-type junction structures. Sci Rep 9(1):14458–14458. https://doi.org/10.1038/s41598-019-50707-x

9. Breitenbach S, Lumetzberger A, Hobisch MA, Unterweger C, Spirk S, Stifter D, Fürst C, Hassel AW (2020) Supercapacitor electrodes from viscose-based activated carbon fibers: significant yield and performance improvement using diammonium hydrogen phosphate as impregnating agent. C J Carbon Res 6(2):17–17. https://doi.org/10.3390/c6020017

10. Breitenbach S, Unterweger C, Lumetzberger A, Duchoslav J, Stifter D, Hassel AW, Fürst C (2021) Viscose-based porous carbon fibers: improving yield and porosity through optimization of the carbonization process by design of experiment. J Porous Mater 28(3):727–739. https://doi.org/10.1007/s10934-020-01026-4

11. Brunner PH, Roberts PV (1980) The significance of heating rate on char yield and char properties in the pyrolysis of cellulose. Carbon 18(3):217–224. https://doi.org/10.1016/0008-6223(80)90064-0

12. Cançado LG, Jorio A, Pimenta MA (2007) Measuring the absolute raman cross section of nanographites as a function of laser energy and crystallite size. Phys Rev B. https://doi.org/10.1103/PhysRevB.76.064304

13. Canevesi RLS, Schaefer S, Izquierdo MT, Celzard A, Fierro V (2022) Roles of surface chemistry and texture of nanoporous activated carbons in CO_2 capture. ACS Appl Nano Mater 5(3):3843–3854. https://doi.org/10.1021/acsanm.1c04474

14. Choi SS, Lee JH, Jin YM, Lee SH (2019) Adsorption characteristics of volatile organic compounds onto lyocell-based activated carbon fibers. Carbon Lett 29(6):633–642. https://doi.org/10.1007/s42823-019-00063-7

15. Cychosz KA, Thommes M (2018) Progress in the physisorption characterization of nanoporous gas storage materials. Engineering 4(4):559–566. https://doi.org/10.1016/j.eng.2018.06.001

16. Dahou T, Defoort F, Khiari B, Labaki M, Dupont C, Jeguirim M (2021) Role of inorganics on the biomass char gasification reactivity: a review involving reaction mechanisms and kinetics models. Renew Sustain Energy Rev 135:110136. https://doi.org/10.1016/j.rser.2020.110136

17. D'Amato D, Veijonaho S, Toppinen A (2020) Towards sustainability? forest-based circular bioeconomy business models in finnish smes. Forest Policy Econ 110:101848–101848. https://doi.org/10.1016/j.forpol.2018.12.004

18. European Parliament (2019) Directive (EU) 2019/904 of the European parliament and of the council of 5 June 2019 on the reduction of the impact of certain plastic products on the environment. Off J L155:1–19

19. Ferrari AC, Robertson J (2000) Interpretation of raman spectra of disordered and amorphous carbon. Phys Rev B 61(20):14095–14107. https://doi.org/10.1103/PhysRevB.61.14095

20. Frank E, Steudle LM, Ingildeev D, Spörl JM, Buchmeiser MR (2014) Carbon fibers: precursor systems, processing, structure, and properties. Angew Chem Int Ed 53(21):5262–5298. https://doi.org/10.1002/anie.201306129

21. Freundlich H (1906) Über die adsorption in Lösungen. Zeitschrift fur Physikalische Chemie 57:385–470

22. Garrido J, Linares-Solano A, Martin-Martinez JM, Molina-Sabio M, Rodriguez-Reinoso F, Torregrosa R (2002) Use of nitrogen vs. carbon dioxide in the characterization of activated carbons. Langmuir 3(1):76–81. https://doi.org/10.1021/la00073a013

23. Haque ANMA, Naebe M (2022) Sustainable biodegradable denim waste composites for potential single-use packaging. Sci Total Environ. https://doi.org/10.1016/j.scitotenv.2021.152239

24. Hina K, Zou H, Qian W, Zuo D, Yi C (2017) Preparation and performance comparison of cellulose-based activated carbon fibres. Cellulose 25(1):607–617. https://doi.org/10.1007/s10570-017-1560-y

25. Huang K, Wang Y (2022) Recent applications of regenerated cellulose films and hydrogels in food packaging. Curr Opin Food Sci 43:7–17. https://doi.org/10.1016/j.cofs.2021.09.003

26. Iacomi P, Llewellyn PL (2019) pyGAPS: a Python-based framework for adsorption isotherm processing and material characterisation. Adsorption 25(8):1533–1542. https://doi.org/10.1007/s10450-019-00168-5

27. Ismail IS, Rashidi NA, Yusup S (2021) Production and characterization of bamboo-based activated carbon through single-step H_3PO_4 activation for CO_2 capture. Environ Sci Pollut Res. https://doi.org/10.1007/s11356-021-15030-x

28. Jaroniec M (1975) Adsorption on heterogeneous surfaces: the exponential equation for the overall adsorption isotherm. Surf Sci 50(2):553–564. https://doi.org/10.1016/0039-6028(75)90044-8

29. Jia SH, Ding X, Yu HT, Han BH (2015) Multi-hydroxyl-containing porous organic polymers based on phenol formaldehyde resin chemistry with high carbon dioxide capture capacity. RSC Adv 5(87):71095–71101. https://doi.org/10.1039/c5ra13405f

30. Karacan I, Soy T (2013) Enhancement of oxidative stabilization of viscose rayon fibers impregnated with ammonium sulfate prior to carbonization and activation steps. J Appl Polym Sci 128(2):1239–1249. https://doi.org/10.1002/app.38496

31. Karacan I, Soy T (2013) Investigation of structural transformations taking place during oxidative stabilization of viscose rayon precursor fibers prior to carbonization and activation. J Mol Struct 1041:29–38. https://doi.org/10.1016/j.molstruc.2013.02.040

32. Karacan I, Soy T (2013) Structure and properties of oxidatively stabilized viscose rayon fibers impregnated with boric acid and phosphoric acid prior to carbonization and activation steps. J Mater Sci 48(5):2009–2021. https://doi.org/10.1007/s10853-012-6970-5

33. Le ND, Trogen M, Ma Y, Varley RJ, Hummel M, Byrne N (2020) Cellulose-lignin composite fibers as precursors for carbon fibers: Part 2 - the impact of precursor properties on carbon fibers. Carbohyd Polym 250(August):116918–116918. https://doi.org/10.1016/j.carbpol.2020.116918

34. Li H, Meng B, Mahurin SM, Chai SH, Nelson KM, Baker DC, Liu H, Dai S (2015) Carbohydrate based hyper-crosslinked organic polymers with -OH functional groups for CO_2 separation. J Mater Chem A 3(42):20913–20918. https://doi.org/10.1039/c5ta03213j

35. Li R, Du J, Zheng Y, Wen Y, Zhang X, Yang W, Lue A, Zhang L (2017) Ultra-lightweight cellulose foam material: preparation and properties. Cellulose 24(3):1417–1426. https://doi.org/10.1007/s10570-017-1196-y

36. Liu A, Li S, Jiang Z, Du J, Tao Y, Lu J, Cheng Y, Wang H (2022) A renewable membrane with high ionic conductivity and thermal stability for Li-ion batteries. J Power Sources. https://doi.org/10.1016/j.jpowsour.2021.230947

37. Liu Y, Wilcox J (2012) Effects of surface heterogeneity on the adsorption of CO_2 in microporous carbons. Environ Sci Technol 46(3):1940–1947. https://doi.org/10.1021/es204071g

38. Lohtander T, Herrala R, Laaksonen P, Franssila S, Österberg M (2022) Lightweight lignocellulosic foams for thermal insulation. Cellulose. https://doi.org/10.1007/s10570-021-04385-6

39. Ma Y, Asaadi S, Johansson LS, Ahvenainen P, Reza M, Alekhina M, Rautkari L, Michud A, Hauru L, Hummel M, Sixta H (2015) High-strength composite fibers from cellulose-lignin blends regenerated from ionic liquid solution. Chemsuschem 8(23):4030–4039. https://doi.org/10.1002/cssc.201501094

40. Mallet-Ladeira P, Puech P, Weisbecker P, Vignoles GL, Monthioux M (2013) Behavior of Raman D band for pyrocarbons with

crystallite size in the 2–5 nm range. Appl Phys A 114(3):759–763. https://doi.org/10.1007/s00339-013-7671-x

41. Mallet-Ladeira P, Puech P, Toulouse C, Cazayous M, Ratel-Ramond N, Weisbecker P, Vignoles GL, Monthioux M (2014) A Raman study to obtain crystallite size of carbon materials: a better alternative to the Tuinstra-Koenig law. Carbon 80:629–639. https://doi.org/10.1016/j.carbon.2014.09.006

42. Marsh H, Rodríguez-Reinoso F (2006) Activated Carbon. Elsevier. https://doi.org/10.1016/B978-0-08-044463-5.X5013-4

43. McCulloch DG, Prawer S, Hoffman A (1994) Structural investigation of xenon-ion-beam-irradiated glassy carbon. Phys Rev B 50(9):5905–5917. https://doi.org/10.1103/PhysRevB.50.5905

44. Miranda-Valdez IY (2022) Non-structural applications of Ioncell® carbon fibers. Master's thesis, Aalto University. School of Chemical Engineering. http://urn.fi/URN:NBN:fi:aalto-202206194011

45. Moriam K, Sawada D, Nieminen K, Hummel M, Ma Y, Rissanen M, Sixta H (2021) Towards regenerated cellulose fibers with high toughness. Cellulose 28(15):9547–9566. https://doi.org/10.1007/s10570-021-04134-9

46. Mubari PK, Beguerie T, Monthioux M, Weiss-Hortala E, Nzihou A, Puech P (2022) The X-ray, Raman and TEM signatures of cellulose-derived carbons explained. J Carbon Res. https://doi.org/10.3390/c8010004

47. Oberlin A (1984) Carbonization and graphitization. Carbon 22(6):521–541. https://doi.org/10.1016/0008-6223(84)90086-1

48. Oelerich J, Bijleveld M, Bouwhuis GH, Brinks GJ (2017) The life cycle assessment of cellulose pulp from waste cotton via the SaXcell™ process. IOP Conf Ser Mater Sci Eng. https://doi.org/10.1088/1757-899x/254/19/192012

49. Ojwang DO, Grins J, Svensson G (2018) The adsorption kinetics of CO_2 on copper hexacyanoferrate studied by thermogravimetric analysis. Microporous Mesoporous Mater 272:70–78. https://doi.org/10.1016/j.micromeso.2018.06.019

50. Oroumei A, Fox B, Naebe M (2015) Thermal and rheological characteristics of biobased carbon fiber precursor derived from low molecular weight organosolv lignin. ACS Sustain Chem Eng 3(4):758–769. https://doi.org/10.1021/acssuschemeng.5b00097

51. Osterrieth J, Rampersad J, Madden DG, Rampal N, Skoric L, Connolly B, Allendorf M, Stavila V, Snider J, Ameloot R, Marreiros J, Ania CO, Azevedo DCS, Vilarrasa-García E, Santos BF, Bu XH, Zang X, Bunzen H, Champness N, Griffin SL, Chen B, Lin RB, Coasne B, Cohen SM, Moreton JC, Colon YJ, Chen L, Clowes R, Coudert FX, Cui Y, Hou B, D'Alessandro D, Doheny PW, Dinca M, Sun C, Doonan C, Huxley M, Evans JD, falcaro p, Riccò R, Farha OK, Idrees KB, Islamoglu T, Feng P, Yang H, Forgan R, Bara D, Furukawa S, Sanchez E, Gascon J, Telalovic S, Ghosha SK, Mukherjee S, Hill MR, Sadiq MM, Horcajada P, Salcedo-Abraira P, Kaneko K, Kukobat R, Kenvin J, Keskin S, Kitagawa S, Otake K, Lively RP, DeWitt SJA, Llewellyn PL, Lotsch B, Emmerling ST, Pütz A, Martí-Gastaldo C, Muñoz N, Garcia-Martinez J, Linares N, Maspoch D, Suarez JA, Moghadam P, Oktavian R, Morris R, Wheatley P, Navarro J, Petit C, Danaci D, Rosseinsky M, Katsoulidis A, Schroder M, Han X, Yang S, Serre C, Mouchaham G, Sholl D, Thyagarajan R, Siderius D, Snurr RQ, Goncalves RB, Telfer SG, Lee SJ, Ting V, Rowlandson J, Uemura T, Iiyuka T, et al (2021) How reproducible are surface areas calculated from the BET equation? Chemrxiv 12:20–25 https://doi.org/10.26434/chemrxiv.14291644.v2

52. Pitkänen L, Sixta H (2020) Size-exclusion chromatography of cellulose: observations on the low-molar-mass fraction. Cellulose 27(16):9217–9225. https://doi.org/10.1007/s10570-020-03419-9

53. Qin C, Lu A (2021) Flexible, anti-freezing self-charging power system composed of cellulose based supercapacitor and triboelectric nanogenerator. Carbohyd Polym. https://doi.org/10.1016/j.carbpol.2021.118667

54. Rampersad J, Osterrieth J, Rampal N (2021) BET surface identification - a program that fully implements the rouquerol criteria. https://github.com/nakulrampal/betsi-gui

55. Reichler M, Rabensteiner S, Törnblom L, Coffeng S, Viitanen L, Jannuzzi L, Mäkinen T, Mac Intyre JR, Koivisto J, Puisto A, Alava MJ (2021) Scalable method for bio-based solid foams that mimic wood. Sci Rep. https://doi.org/10.1038/s41598-021-03764-0

56. Reyes-Melo ME, Miranda-Valdez IY, Puente-Córdova JG, Camarillo-Hernández CA, López-Walle B (2021) Fabrication and characterization of a biocompatible hybrid film based on silver nanoparticle/ethyl cellulose polymer. Cellulose 28(14):9227–9240. https://doi.org/10.1007/s10570-021-04066-4

57. Rouquerol J, Avnir D, Fairbridge CW, Everett DH, Haynes JM, Pernicone N, Ramsay JDF, Sing KSW, Unger KK (1994) Recommendations for the characterization of porous solids (technical report). Pure Appl Chem 66(8):1739–1758. https://doi.org/10.1351/pac199466081739

58. Scholz R, Herbig F, Beck D, Spörl J, Hermanutz F, Unterweger C, Piana F (2019) Improvements in the carbonisation of viscose fibres. Reinf Plast 63(3):146–150. https://doi.org/10.1016/j.repl.2018.10.002

59. Sevilla M, Valle-Vigón P, Fuertes AB (2011) N-doped polypyrrole-based porous carbons for CO_2 capture. Adv Func Mater 21(14):2781–2787. https://doi.org/10.1002/adfm.201100291

60. Sherwood J (2020) The significance of biomass in a circular economy. Biores Technol 300:122755–122755. https://doi.org/10.1016/j.biortech.2020.122755

61. Shi H (1996) Activated carbons and double layer capacitance. Electrochim Acta 41(10):1633–1639. https://doi.org/10.1016/0013-4686(95)00416-5

62. Sixta H, Michud A, Hauru L, Asaadi S, Ma Y, King AWT, Kilpeläinen I, Hummel M (2015) Ioncell-f: a high-strength regenerated cellulose fibre. Nord Pulp Pap Res J 30(1):43–57. https://doi.org/10.3183/npprj-2015-30-01-p043-057

63. Smith MW, Dallmeyer I, Johnson TJ, Brauer CS, McEwen JS, Espinal JF, Garcia-Perez M (2016) Structural analysis of char by Raman spectroscopy: improving band assignments through computational calculations from first principles. Carbon 100:678–692. https://doi.org/10.1016/j.carbon.2016.01.031

64. Stegmann P, Londo M, Junginger M (2020) The circular bioeconomy: its elements and role in European bioeconomy clusters. Resour Conserv Recycl X 6:100029–100029. https://doi.org/10.1016/j.rcrx.2019.100029

65. Tan XF, Liu SB, Liu YG, Gu YL, Zeng GM, Hu XJ, Wang X, Liu SH, Jiang LH (2017) Biochar as potential sustainable precursors for activated carbon production: multiple applications in environmental protection and energy storage. Biores Technol 227:359–372. https://doi.org/10.1016/j.biortech.2016.12.083

66. Tang M, Bacon R (1964) Carbonization of cellulose fibers-I. Low temperature pyrolysis. Carbon 2(3):211–220. https://doi.org/10.1016/0008-6223(64)90035-1

67. TENCEL official site: Lyocell fibers, modal fibers, soft fabric textile. (n.d.). https://www.tencel.com/

68. Thommes M, Kaneko K, Neimark AV, Olivier JP, Rodriguez-Reinoso F, Rouquerol J, Sing KSW (2015) Physisorption of gases, with special reference to the evaluation of surface area and pore size distribution (iupac technical report). Pure Appl Chem 87(9–10):1051–1069. https://doi.org/10.1515/pac-2014-1117

69. Trifol J, Moriana R (2022) Barrier packaging solutions from residual biomass: synergetic properties of cnf and lcnf in films. Ind Crops Prod. https://doi.org/10.1016/j.indcrop.2021.114493

70. Trogen M, Le ND, Sawada D, Guizani C, Lourençon TV, Pitkänen L, Sixta H, Shah R, O'Neill H, Balakshin M, Byrne N, Hummel M (2021) Cellulose-lignin composite fibres as precursors for carbon fibres. Part 1 - manufacturing and properties of precursor fibres.

Carbohyd Polym 252(September 220):117133–117133. https://doi.org/10.1016/j.carbpol.2020.117133

71. Wang Q, Wang W, Huang J, Yin H, Zhu Y, Wang H, Zhou M, He B, Hou Z, Xu W (2023) A simple electrospinning strategy to achieve the uniform distribution of ultra-fine CoP nanocrystals on carbon nanofibers for efficient lithium storage. Carbon Lett 33(1):203–213. https://doi.org/10.1007/s42823-022-00417-8

72. Wu H, Thibault CG, Wang H, Cychosz KA, Thommes M, Li J (2016) Effect of temperature on hydrogen and carbon dioxide adsorption hysteresis in an ultramicroporous mof. Microporous Mesoporous Mater 219:186–189. https://doi.org/10.1016/j.micromeso.2015.08.005

73. Wu H, Gakhar R, Chen A, Lam S, Marshall CP, Scarlat RO (2020) Comparative analysis of microstructure and reactive sites for nuclear graphite IG-110 and graphite matrix A3. J Nucl Mater. https://doi.org/10.1016/j.jnucmat.2019.151802

74. Yang M, Chen Y, Wang H, Zou Y, Wu P, Zou J, Jiang J (2022) Solvothermal preparation of CeO_2 nanoparticles-graphene nanocomposites as an electrochemical sensor for sensitive detecting pentachlorophenol. Carbon Lett. https://doi.org/10.1007/s42823-022-00353-7

75. Yang M, Zou Y, Ding L, Yu Y, Ma J, Li L, Rafryanto AF, Zou J, Arramel Wang H (2023) TiO_2 nanoparticles anchored on graphene oxide nanosheets as a highly active photocatalyst for decabromodiphenyl ether degradation. Carbon Lett. https://doi.org/10.1007/s42823-022-00456-1

76. Zeng F, Pan D (2008) The structural transitions of rayon under the promotion of a phosphate in the preparation of ACF. Cellulose 15(1):91–99. https://doi.org/10.1007/s10570-007-9148-6

77. Zhang X, Dong S, Wu W, Yang J, Li J, Shi K, Liu H (2020) Influence of lignin units on the properties of lignin/ PAN-derived carbon fibers. J Appl Polym Sci. https://doi.org/10.1002/app.49274

78. Zheng J, Zhao Q, Ye Z (2014) Preparation and characterization of activated carbon fiber (ACF) from cotton woven waste. Appl Surf Sci 299:86–91. https://doi.org/10.1016/j.apsusc.2014.01.190

79. Zolkin PI, Cheblakova EG, Aberyakhimov KI, Tatarinov VF (2011) Development of biocompatible carbon fibers from hydrated cellulose for the treatment of glaucoma. Solid Fuel Chem 45(5):359–362. https://doi.org/10.3103/S0361521911050144

Authors and Affiliations

Isaac Y. Miranda-Valdez[1] [ORCID] · **Chamseddine Guizani[1,2]** · **Nathalie Abbrederis[1]** · **Mikaela Trogen[1]** · **Michael Hummel[1]**

✉ Isaac Y. Miranda-Valdez
isaac.mirandavaldez@aalto.fi

Chamseddine Guizani
chamseddine.guizani@vtt.fi

Michael Hummel
michael.hummel@aalto.fi

[1] Department of Bioproducts and Biosystems, School of Chemical Engineering, Aalto University, 02150 Espoo, Finland

[2] VTT Technical Research Centre of Finland Ltd, VTT, P.O. Box 1000, FI-02044 Espoo, Finland